Journal of Solid State Chemistry 184 (2011) 2978–2986

Contents lists available at SciVerse ScienceDirect

Journal of Solid State Chemistry

journal homepage: www.elsevier.com/locate/jssc

Apatite metaprism twist angle (φ) as a tool for crystallochemical diagnosis

S.C. Lim [a,*], Tom Baikie [a], Stevin S. Pramana [a], Ron Smith [b], T.J. White [a,c]

[a] Nanyang Technological University, School of Materials Science and Engineering, 50 Nanyang Avenue, Singapore 639798, Singapore
[b] ISIS User Office, Building R3, Rutherford Appleton Laboratory, Chilton, Didcot, OXON OX11 OQX, United Kingdom
[c] Centre for Advanced Microscopy, Australian National University, Canberra, ACT 2601, Australia

ARTICLE INFO

Article history:
Received 12 May 2011
Received in revised form
27 July 2011
Accepted 22 August 2011
Available online 1 September 2011

Keywords:
Metaprism twist angle
Apatite crystal chemistry
Neutron diffraction

ABSTRACT

$[A^{I}]_4[A^{II}]_6(BO_4)_6X_2$ apatites can flexibly accommodate numerous cationic, metalloid and anionic substitutions. Using a combination of new refinements and published structures, this paper reviews correlations between substituent type and framework adaptation through adjustment of the $A^{I}O_6$ metaprism twist angle, φ. These systematics are illustrated through powder neutron diffraction refinement of the crystal chemistry of $A_{10}(PO_4)_6F_2$ (A=Ca, Sr) fluorapatites. Variations in φ reflect changes in the relative size of the $A^{I}_4(BO_4)_6$ framework and $A^{II}_6X_2$ tunnel content and can be used to quantitatively assess the reliability of A^{I}/A^{II} cation partitioning coefficients determined by Rietveld analysis. In the simplest cases of bi-ionic substitution, the metaprism twist systematics conform to three principle trends

(i) For A-type divalent substitution, the larger A^{2+} species preferentially enters the channel before partitioning to the framework. This leads to parabolic modification in φ across the compositional series;
(ii) For B-type pentavalent compounds, the φ variation will be linear in accord with the relative B^{5+} ionic size; and
(iii) For X-type substitution of halide anions, φ will be reduced as the average size increases.

Departures from these trends may indicate polymorphism, compositional anomalies, A^{I}/A^{II} order disequilibrium, or poor structure refinement, and may be extended to chemically complex apatites with simultaneous substitutions over the A, B and X sites.

1. Introduction

The apatites are a chemically diverse crystallographic family used as prosthesis materials [1] and for drug release [2], in clean energy delivery [3] and heterogeneous catalysis [4], and for the remediation of hazardous [5] and nuclear wastes [6]. The essential features of the apatite group were established by the structure determination of the holotype $Ca_{10}(PO_4)_6(OH,F)_2$ [7,8] and the synthesis of several chemical analogues including $Ca_{10}(PO_4)_6Br_2$, $Ca_{10}(VO_4)_6I_2$ and $Cd_{10}(VO_4)_6Cl_2$ [9]. In general, these compounds conform to hexagonal $P6_3/m$ symmetry reflected in the formula $[A^{I}_4][A^{II}_6](BO_4)_6X_2$, although the non-isomorphic subgroups are more common than often supposed [10]. Moreover, non-stoichiometry is readily accommodated, especially with respect to the X anion, but compositional disparities are sometimes poorly documented due to difficulties in establishing site occupancy by powder diffraction methods [11] and the absence of supporting chemical and spectroscopic analyses or single crystal diffraction data [12,13]. In some circumstances, especially plumbous compositions, polysomatism may appear through rotational twinning leading to 3H and 4H forms in addition to the 2H prototype [14].

Systematisation of apatite crystal chemistry is essential to tailor functionality for specific technologies, but devising a classification scheme requires access to reliable crystal structures. While single crystal determinations are preferable, Rietveld refinement is used extensively because model structures are easily devised and many apatites are most readily synthesised as powders. However, the least-squares procedure can lead to false minima due to the propagation of errors during matrix inversion [15]. Nonetheless, the accuracy and numerical stability of Rietveld analysis can be enhanced either by applying soft constraints to the BO_4 tetrahedra [16] or controlling atomic trajectories through introducing geometrical parameterisations [11], and are particularly valuable for locating oxygen within the relatively fixed $D8_8$ cation sub-lattice of apatite [17].

While these techniques can be applied to new refinements, it would be useful to possess a quantitative means to assess the existing body of reported apatite structures in a manner that goes

* Corresponding author. Fax: +65 6790 9081.
E-mail address: lims0051@e.ntu.edu.sg (S.C. Lim).

0022-4596/$ - see front matter © 2011 Elsevier Inc. All rights reserved.
doi:10.1016/j.jssc.2011.08.031

beyond a conventional analysis of bond lengths and angles. One approach is to consider apatites as one-dimensional channel structures in which a framework, composed of face-sharing $A^{I}O_6$ metaprism columns corner-connected to BO_4 tetrahedra, hosts the $A^{II}_6X_2$ component (Fig. 1). The tunnel diameter adjusts according to the size (of A^{II} and X) and stoichiometry (X) of its contents by counter-rotation of the opposing triangular faces of the metaprism through a [0 0 1] projected angle (φ) and the extent of metaprism twisting varies inversely with tunnel cross section. For $P6_3/m$ structures $5^\circ \le \varphi \le 25^\circ$, and when apatites contain the same A-component, but different B and X constituents, there is a linear relationship between φ and the average crystal radii [18]. Metaprism twisting is established through the O(1) and O(2) positions, that together with O(3), form the semi-rigid framework BO_4 tetrahedron whose location is determined through bonding to the A^{II} tunnel cation. Because φ arises from the interplay between several atoms, this single parameter proves exquisitely sensitive to crystallochemical variations. Across a solid solution series deviations from trend usually reflect departures from nominal stoichiometry, polymorphism (2*H*, 2*T*, 2*M*, 2*A* for di-modular stacking) or poor structure refinement.

The present work is directed towards the accurate determination of φ in $[Sr_{10-x}Ca_x][(PO_4)_6][F_2]$ 2*H* apatites. The data are compared with several published crystallographic data sets, which through an evaluation of φ, serve to emphasise the generality of twist angle systematics, and the diagnostic potential for assessing the reliability of Rietveld refinements and detecting disequilibrium and non-stoichiometry.

2. Experimental methods

2.1. Synthesis of $[Sr_{10-x}Ca_x][(PO_4)_6][F_2]$

The starting materials were calcium nitrate ($Ca(NO_3)_2 \cdot 4H_2O$-Aldrich, 99%), strontium nitrate ($Sr(NO_3)_2$-Acros, 99%), ammonium hydrogen phosphate ($(NH_4)_2HPO_4$-Aldrich, 99%) and ammonium fluoride (NH_4F-Acros, 98%). The synthesis is a modified version of the route developed by Collin [19,20] and required two stock solutions. In Solution I, calcium nitrate and strontium nitrate were dissolved in 100 ml of deionised water at 85 °C while maintaining a cation concentration of 0.2 M. Ammonia was added to raise the pH above 10. In Solution II, ammonium hydrogen phosphate 1.6007 g (0.2 M) and ammonium fluoride 0.3024 g (0.13 M) were dissolved in 60 ml of deionised water and the pH adjusted by ammonia to be >10. Solution II was added drop-wise to Solution I with heating and stirring to obtain a total volume of approximately 200 ml. The precipitate and solution were maintained at 85 °C with stirring for 3 h and filtered while warm. The solid was dried overnight at 100 °C then calcined at 700 °C for 6 h under flowing nitrogen.

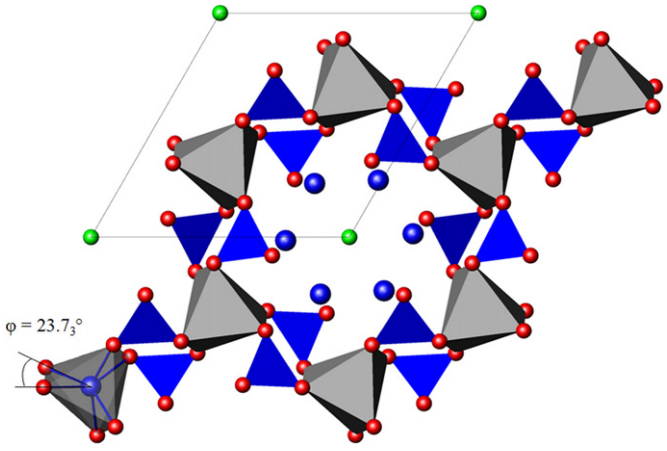

Fig. 1. Polyhedral representation of $Sr_{10}(PO_4)_6F_2$.

2.2. Characterisation

Powder X-ray diffraction (PXRD) patterns were collected using a Shimadzu LabX XRD-6000 with Cu$K\alpha$ radiation step-scanned from 10° to 140° 2θ at intervals of 0.02°, with a total collection time of approximately 12 h. The intensity of the strongest peak ranged from 5000 to 18,000 counts and the whole patterns were analysed by Rietveld refinement using *TOPAS V3* [21] that employs the fundamental parameters approach [22]. Refinement parameters included the zero point error, a 4 coefficient Chebychev polynomial background fitting, and 'crystallite size' to simulate microstructure-controlled line broadening. To maintain reasonable *B*–O bond lengths within the BO_4 units a 'Parabola *N*' penalty function was employed with expected bond lengths selected in accordance with standard ionic radii [23]. Powder neutron diffraction (PND) patterns for $[Sr_{10-x}Ca_x][(PO_4)_6][F_2]$ were collected at the ISIS Rutherford Appleton Laboratory on the medium resolution Polaris beamline [24]. Approximately 1–2 cm^3 of each apatite powder was loaded into 8 mm diameter vanadium cans. Data sets from two banks of detectors were combined for the refinement; the first from the backscattering detector bank (average $2\theta \approx 145^\circ$) and the second from the 90° detector bank. Rietveld refinements were performed with *GSAS* [25]. As expected, neutron diffraction refinements were more robust for determining oxygen positions and bond-length constraints were unnecessary.

The quality of the Rietveld refinements was checked by calculating the metaprism twist angle using the method of White and Dong [18]. For a given metaprism, a consideration of the absolute fractional atomic co-ordinates (x, y) of A^{I}, O(1) and O(2) allows φ to be calculated as

$$\cos\varphi = \frac{\left[(G_3-G_1)^2+(H_3-H_1)^2+(G_1-G_2)^2+(H_1-H_2)^2-(G_2-G_3)^2-(H_2-H_3)^2\right]}{2\times\sqrt{\left[(G_3-G_1)^2+(H_3-H_1)^2\right]\times\left[(G_1-G_2)^2+(H_1-H_2)^2\right]}}$$

where $G_1=0.866x_{AI}$, $H_1=y_{AI}-0.5x_{AI}$, $G_2=0.866x_{O1}$, $H_1=y_{O1}-0.5x_{O1}$ and $G_3=0.866x_{O2}$, $H_1=y_{O2}-0.5x_{O2}$.

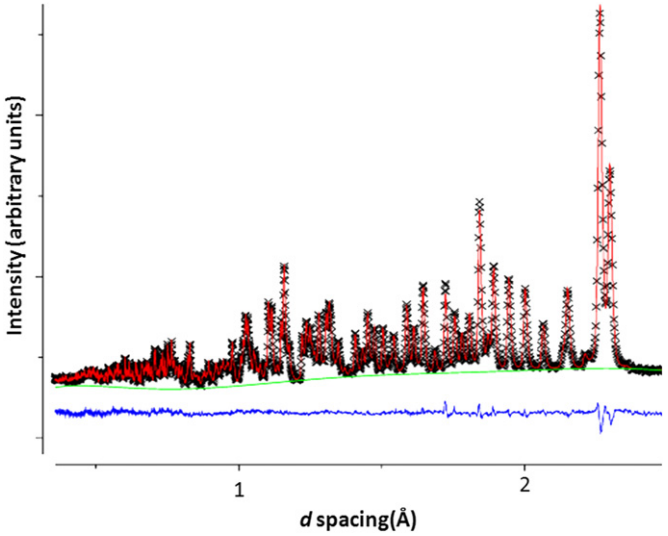

Fig. 2. Rietveld profile of PND for $Ca_{10}(PO_4)_6F_2$. Observed counts are shown in crosses, the calculated pattern by a solid black line, background in green, and the difference in blue. (For interpretation of the references to colour in this figure legend, the reader is referred to the web version of this article.)

3. Results

Powder X-ray diffraction confirmed the synthesis of the entire solid-solution series. Rietveld refinements used the model structures of Nikčević et al. [26], and Swafford and Holt [27] with appropriate chemical substitutions. For all samples PXRD and PND converged to comparable lattice parameters. The atomic positions and selected bond lengths from the neutron refinements all lie within expected ranges (Tables 1 and 2 and supplementary Table A1), and vary appropriately with the Ca/Sr substitution. The lattice parameters are in good agreement with previous work [19,20,28,29], and c/a lies in the range 0.732–0.745 as found by Pujari and Patel [30]. The cell edges dilate linearly (Fig. 3) as strontium is introduced because Sr^{2+} (1.18 Å) is larger than Ca^{2+} (1.00 Å) [23], confirming the solid solution is homogeneous. The oxygen and fluorine positions were refined from neutron data using anisotropic displacement parameters as the fitting was superior. As little improvement was found when the Ca/Sr and P sites were refined with anisotropic displacement parameters, these were treated isotropically to minimise the number of refinement parameters while yielding comparable residual values (Fig. 2, Tables 1 and 2 and supplementary Table A1).

Table 2
Selected bond length and angles for the $[Sr_{10-x}Ca_x][(PO_4)_6][F_2]$ series.

Composition x	0	2.56	5	7.56	10
Bond length (Å)					
A(1)–O(1)	2.5544(9)	2.5140(18)	2.4806(14)	2.4409(14)	2.4038(9)
A(1)–O(2)	2.5722(8)	2.5277(17)	2.4938(14)	2.4634(14)	2.4513(9)
A(1)–O(3)	2.9033(7)	2.8796(17)	2.8556(13)	2.8275(12)	2.8027(7)
A(2)–O(1)	2.7350(11)	2.732(2)	2.741(2)	2.735(2)	2.6828(14)
A(2)–O(2)	2.5058(12)	2.495(2)	2.4821(19)	2.4282(19)	2.3821(13)
A(2)–O(3)	2.5263(6)	2.4837(12)	2.4444(9)	2.3968(9)	2.3534(6)
	2.6575(9)	2.651(2)	2.6202(17)	2.5450(18)	2.4993(12)
A(2)–F	2.4007(8)	2.3745(17)	2.3477(13)	2.3102(14)	2.2917(10)
P–O(1)	1.5411(12)	1.518(2)	1.5245(18)	1.5223(16)	1.5279(10)
P–O(2)	1.5381(12)	1.535(3)	1.5286(18)	1.5369(17)	1.5333(11)
P–O(3)	1.5342(7)	1.5288(14)	1.5282(11)	1.5241(10)	1.5256(7)
Angle (deg.)					
O(1)–P–O(3)	110.63(4)	110.78(9)	110.62(7)	110.77(7)	110.84(4)
O(1)–P–O(2)	110.87(7)	111.99(16)	111.87(12)	111.43(11)	111.26(7)
O(3)–P–O(3)	108.15(7)	107.57(16)	108.02(11)	108.08(10)	107.58(7)
O(3)–P–O(2)	108.23(5)	107.77(10)	107.78(7)	107.83(7)	108.09(5)

Table 1
Lattice parameters and crystallographic data for the $[Sr_{10-x}Ca_x][(PO_4)_6][F_2]$ series.

Composition x	0	2.56	5.00	7.56	10.00
Space Group	$P6_3/m$	$P6_3/m$	$P6_3/m$	$P6_3/m$	$P6_3/m$
a (Å)	9.71333(6)	9.6298(2)	9.56211(13)	9.45877(13)	9.36723(7)
c (Å)	7.28428(7)	7.1826(3)	7.09772(16)	6.97565(14)	6.88445(8)
V (Å^3)	595.187(6)	576.83(2)	562.027(14)	540.486(14)	523.145(8)
φ (deg.)	23.7_3	22.6_5	22.2_7	22.5_7	23.5_2
k_{Sr} (A^I/A^{II})[b]	0.67	0.64	0.46	0.45	~
R_{wp}	0.0158	0.0188	0.0177	0.0162	0.0149
R_p	0.0322	0.0376	0.0336	0.0323	0.0271
Sr(1), 4f (1/3, 2/3, z)					
z	−0.00005(12)	0.0002(3)	0.0001(2)	−0.0002(2)	0.00052(16)
Occ. Fac. (Sr)	1	0.73(2)	0.396(12)	0.190(16)	0
U_{iso}	0.00636(13)	0.0065(4)	0.0080(3)	0.0089(4)	0.00697(17)
Sr(2), 6h (x, y, 1/4)					
x	0.23921(9)	0.2383(2)	0.23828(17)	0.23979(19)	0.24063(13)
y	−0.01519(8)	−0.01579(19)	−0.01389(16)	−0.0087(2)	−0.00785(14)
Occ. Fac. (Sr)	1	0.753(16)	0.570(8)	0.280(11)	0
U_{iso}	0.00604(11)	0.0053(3)	0.0094(3)	0.0116(3)	0.00756(16)
P, 6h (x, y, 1/4)					
x	0.39953(11)	0.4008(2)	0.40143(18)	0.39965(17)	0.39833(11)
y	0.36845(10)	0.3712(2)	0.37100(16)	0.36988(15)	0.36886(10)
U_{iso}	0.00407(12)	0.0043(2)	0.00680(19)	0.00673(18)	0.00491(12)
O(1), 6h (x, y, 1/4)					
x	0.33046(10)	0.3330(2)	0.33391(16)	0.33100(14)	0.32671(9)
y	0.48086(10)	0.4836(2)	0.48557(17)	0.48511(15)	0.48391(10)
U_{iso}	0.00793[a]	0.00934[a]	0.01315[a]	0.01118[a]	0.00818[a]
O(2), 6h (x, y, 1/4)					
x	0.58233(9)	0.58485(19)	0.58602(14)	0.58727(13)	0.58730(8)
y	0.46337(10)	0.4629(2)	0.46231(17)	0.46439(17)	0.46645(11)
U_{iso}	0.00929[a]	0.01651[a]	0.01838[a]	0.01508[a]	0.01044[a]
O(3), 12i (x, y, z)					
x	0.34452(9)	0.3446(2)	0.34451(15)	0.34309(14)	0.34172(9)
y	0.26146(8)	0.26292(18)	0.26261(13)	0.26065(12)	0.25777(8)
z	0.07944(7)	0.07827(16)	0.07579(12)	0.07315(10)	0.07121(7)
U_{iso}	0.01097[a]	0.01601[a]	0.01862[a]	0.01735[a]	0.01252[a]
F(1), 2a (0, 0, 1/4)					
U_{iso}	0.0233[a]	0.03431[a]	0.03828[a]	0.03431[a]	0.01837[a]

[a] See table of anisotropic displacement parameters in supplementary details section.
[b] k_{Sr} (A^I/A^{II})=(2∗Occ. Fac. Sr(1))/(3∗Occ. Fac. Sr(2)); Equal partitioning of Sr over A^I and A^{II} leads to k_{Sr}=0.67.

3.1. Twist angle (φ) systematics and 'anomalies'

3.1.1. A-site correlations in $[Sr_{10-x}Ca_x][(PO_4)_6][F_2]$ and other apatites

In this work, the metaprism twist angles in $[Sr_{10-x}Ca_x][(PO_4)_6][F_2]$ show parabolic behaviour as x increases due to the non-statistical distribution of alkali earths across the 4*f* and 6*h* sites. At lower concentration, Sr^{2+} initially prefers the larger 6*h* sites, causing the tunnel to expand and φ to become more acute (Fig. 4). However, once the 6*h* site is more completely occupied by strontium, φ increases as more Sr^{2+} partitions to the 4*f* site. For the end-members, the relative sizes of the framework and tunnel are similar and the metaprism twisting is comparable as evidenced by comparing φ for $Ca_{10}(PO_4)_6(OH)_2$ ($\varphi = 23.2_1^\circ$) and $Sr_{10}(PO_4)_6(OH)_2$ (22.8_3°); $Ba_{10}(PO_4)_6(OH)_2$ yields similar φ (22.2_0°) because the *A*-sites are isovalent (Table 3). Separately, Michie et al. [40] showed with quantum mechanical simulations for $[Sr_{10-x}Ca_x][(PO_4)_6][F_2]$ that internal energy calculations conform to a similar parabolic distribution. This behaviour is general for isovalent *A*-site substitutions in apatites, as for example, in $[Ba_{10-x}Sr_x][(PO_4)_6][F_2]$ [36] (Tables 3 and 4, Fig. 4). Whenever there is a size difference between *A* species of the same valence, the larger ion will preferentially enter the 6*h* tunnel position rather than the 4*f* framework site leading to a parabolic φ trend.

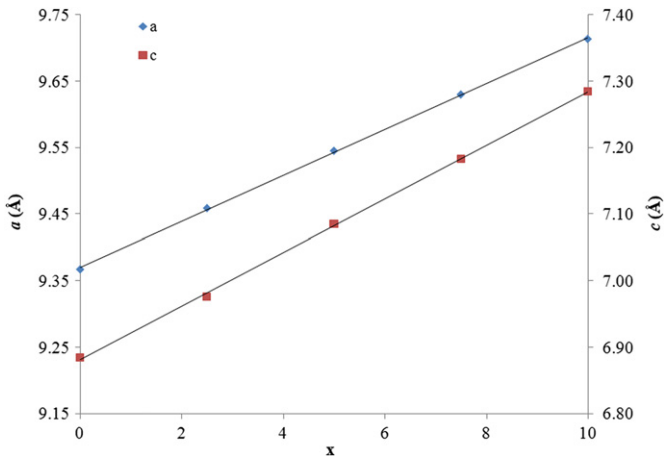

Fig. 3. Lattice parameters for $[Sr_{10-x}Ca_x][(PO_4)_6][F_2]$ derived from powder neutron diffraction where *a* and *c* are diamonds and squares, respectively.

The A^I/A^{II} partitioning coefficient in $[A^I_4][A^{II}_6](BO_4)_6X_2$ can be expressed as

$$k_A(A^I/A^{II}) = (2*\text{Occ. Fac.}A^I/(3*\text{Occ. Fac.}A^{II}) \quad (1)$$

Equal partitioning of *A* over A^I and A^{II} leads to $k_A = 0.67$. k_{Sr} (A^I/A^{II}) in $[Sr_{10-x}Ca_x][(PO_4)_6][F_2]$ and k_{Ba} (A^I/A^{II}) in $[Ba_{10-x}Sr_x][(PO_4)_6][F_2]$ [36] are below 0.67, suggesting that Sr^{2+} in the former and Ba^{2+} in the latter occupy 6*h* preferably rather than 4*f* site. The lower values of k_{Ba} for the $[Ba_{10-x}Sr_x][(PO_4)_6][F_2]$ series reflects the stronger partitioning of the larger Ba for the 6*h* site which leads to the greater variation in twist angle (see Tables 1 and 4).

This simple rule will not be applicable if there are mixtures of higher valence cations (e.g. rare earth^{3+}) or monovalent species (e.g. Na^+); the former prefer 6*h* to better distribute higher charge, while the reverse is true for large monovalent cations. Ionic charge always takes precedence over size.

These prescriptions to predict A^I/A^{II} site partitioning assume bonding is predominantly ionic in nature. However, cadmium appears to behave in a different fashion. On the basis of size it would be expected in $[Ca_{10-x}Cd_x][(PO_4)_6][(OH)_2]$ apatite that Cd^{2+} (IR = 0.95 Å) would displace Ca^{2+} (IR = 1.00 Å) in the smaller A^I framework site. In fact, several studies [41,42] suggest that Cd^{2+} preferentially occupies the tunnel (6*h* site). Most recently, Terra et al. [43] used a combination of computation and synchrotron powder diffraction to propose that the significantly greater covalent character

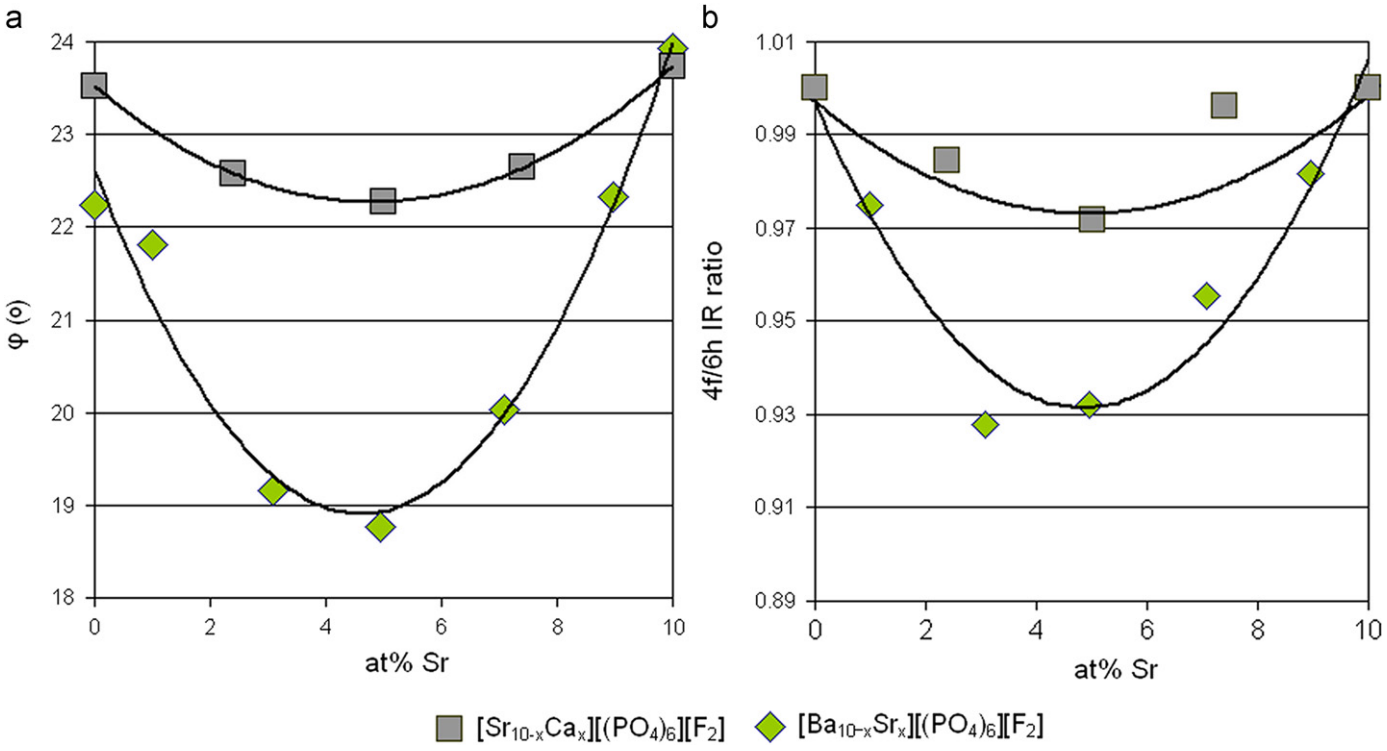

Fig. 4. Comparison of crystallochemical trends for $[Sr_{10-x}Ca_x][(PO_4)_6][F_2]$ (this study) and $[Ba_{10-x}Sr_x][(PO_4)_6][F_2]$ [36]. (a) The metaprism twist angle (φ) varies in a parabolic fashion due to the distribution A^I/A^{II} cations that continuously adjust the diameter of the framework. (b) The relative size of the framework (4*h*) cations to tunnel (6*h*) cations follows the same behaviour.

Table 3
Trends and anomalies in metaprism twist angle variance for $[A_{10}][(BO_4)_6][X_2]$ apatites.

Substitution type	Compound	φ (deg.)	Unit Cell Volume (Å^3)	Twist angle systematics	Reference
***A*-type**	$Ca_{10}(PO_4)_6F_2$	24.3_5	523.63	Sr^{2+} preferentially fills the tunnels, before entering the framework. The size of the framework with respect to the tunnel is minimised at intermediate Ca/Sr compositions with the channel dilating by reducing φ. For the end-members, the relative sizes of the framework and tunnel are similar and the metaprism twists are comparable.	This Work
	$Ca_{6.66}Sr_{3.34}(PO_4)_6F_2$	22.9_5	545.37		
	$Ca_{4.02}Sr_{5.98}(PO_4)_6F_2$	21.6_6	559.16		
	$Ca_{1.66}Sr_{8.34}(PO_4)_6F_2$	21.4_6	573.33		
	$Sr_{10}(PO_4)_6F_2$	23.9_5	596.14		
	$Ca_{10}(PO_4)_6(OH)_2$	23.2_1	528.67	The twist angles for Ca^{2+} and Sr^{2+} hydroxy and fluoro apatites are similar as the *X* anion (F^-/OH^-) occupy nearly the same volumes. Ba^{2+} apatite yields similar φ as the relative size of framework are similar because the *A*-sites are homoatomic.	Sudarsanan and Young [29]
	$Sr_{10}(PO_4)_6(OH)_2$	22.8_3	597.49		
	$Ba_{10}(PO_4)_6(OH)_2$	22.2_0	694.29		
	$Ca_{10}(PO_4)_6Cl_2$	17.8_6	544.50	The twist angles for chloro apatites are less than fluro and hydroxyl analogues as Cl^- is a substantially larger *X* anion, with the tunnel opening by decreasing φ. While following the parabolic trend for differential Ca/Sr site partitioning, φ for $Ca_{10}(PO_4)_6Cl_2$ appears to be anomalously small compared to the $Sr_{10}(PO_4)_6Cl_2$ end-member. In fact, this reflects a change in symmetry from $P6_3/m$ to $P2_1/b$. In the original refinement of chlorapatite [9] the symmetry was taken as $P6_3/m$ which lead to $\varphi = 19.1^\circ$.	Sudarsanan and Young [31]
	$Ca_{9.8}Sr_{0.2}(PO_4)_6Cl_2$	17.4_6	545.20		
	$Ca_{9.5}Sr_{0.5}(PO_4)_6Cl_2$	17.1_8	546.40		
	$Ca_5Sr_5(PO_4)_6Cl_2$	16.8_3	576.50		
	$Sr_{10}(PO_4)_6Cl_2$	21.1_0	606.60		
	$Ca_{9.95}Sr_{0.05}(PO_4)_6(OH)_2$	22.2_8	532.29	The twist angles for $Ca_9Sr_1(PO_4)_6(OH)_2$ and $Ca_5Sr_5(PO_4)_6(OH)_2$ grow larger as the compounds become increasingly strontium rich when the opposite behaviour is expected due the favoured introduction of Sr to the tunnel. In this case, oxidation of the *X* anion ($2OH^- \rightarrow O^{2-} + \square$) creates tunnel vacancies with a corresponding reduction in diameter and increase in φ.	Bigi et al. [28]
	$Ca_9Sr_1(PO_4)_6(OH)_2$	22.5_2	533.89		
	$Ca_5Sr_5(PO_4)_6(OH)_2$	22.4_6	570.43		
	$Ca_8Pb_2(PO_4)_6(OH)_2$	16.1_3	542.41	Pb^{2+} is driven towards tunnel positions as it is larger than Ca^{2+}, and in addition, requires space to accommodate stereochemically active lone pair electrons. Parabolic φ trend is as expected.	Bigi et al. [32]
	$Ca_{5.5}Pb_{4.5}(PO_4)_6(OH)_2$	13.7_0	565.90		
	$Ca_2Pb_8(PO_4)_6(OH)_2$	18.1_3	604.98		
	$Na_2Pb_8(VO_4)_6\square_2$	26.1_7	643.84	In lacunar apatites, tunnels are devoid of *X* anions ($X = \square$). As the tunnel is vacated it must constrict and this is achieved by increasing φ. These compounds show the largest φ of all $[A_{10}][(BO_4)_6][X_2]$ apatites.	Azrour et al. [33] Koumiri et al. [34]
	$K_2Pb_8(VO_4)_6\square_2$	29.0_3	659.41		
	$Na_2Pb_8(PO_4)_6\square_2$	24.0_2	588.88		
	$Ca_5Pb_5(VO_4)_6F_2$	14.4 (equilibrated)	616.70	Apatite *A*-site ordering and/or compositions can change with annealing. For the non-equilibrated $Ca_5Pb_5(VO_4)_6F_2$ annealed for 1 day the nominal composition is correct but the Ca/Pb are distributed statistically over the *A* sites, the average *A* cation size over the framework and tunnel are the same, and $\varphi = 22^\circ$ is similar to other homoatomic *A*-site apatites e.g. $Sr_{10}(PO_4)_6F_2$. After long annealing (1 week) Ca/Pb order is established, the framework is small relative to the tunnel and φ is small to dilate the channel. In this case, there is some loss of fluorine ($2F^- \rightarrow O^{2-} + \square$) which would tend to increase φ, but this is less significant than Ca/Pb ordering.	Dong and White [35]
	$Ca_5Pb_5(VO_4)_6F_2$	22.0 (non-equilibrated)	624.04		
	$Ba_{10}(PO_4)_6F_2$	22.2_3	691.38	Whenever the is a size difference between *A* species of the same valence the larger ion will preferentially enter the 6*h* tunnel position rather than the 4*f* framework site leading to a parabolic φ trend. This simple rule will not be applicable if there are higher valence cations (e.g. RE^{3+}) or monovalent species (e.g. Na^+); the former prefer 6*h* to better distribute higher charge while the reverse is true for large monovalent cations. Charge considerations will always take precedence over size.	Aissa et al. [36]
	$Ba_{9.01}Sr_{0.99}(PO_4)_6F_2$	21.8_1	680.32		
	$Ba_{6.92}Sr_{3.08}(PO_4)_6F_2$	19.1_6	665.06		
	$Ba_{5.05}Sr_{4.95}(PO_4)_6F_2$	18.7_6	639.39		
	$Ba_{2.92}Sr_{7.08}(PO_4)_6F_2$	20.0_3	619.35		
	$Ba_{1.03}Sr_{8.97}(PO_4)_6F_2$	22.3_3	604.79		
	$Sr_{10}(PO_4)_6F_2$	23.9_3	596.35		

***B*-type**	$Ca_{10}(PO_4)_6(OH)_2$	23.4_8	529.81	For $Ca_{10}(P_{1-x}As_xO_4)_6(OH)_2$ apatites the twist angle increases as larger As^{5+} displaces P^{5+} as expected. However, at the highest As concentrations φ reverses trend. This is an indicator that the structure is undergoing additional modification. It is believed the arsenous compounds are triclinic and may be isostructural with $Ca_{10}(AsO_4)_6F_2$	Lee et al. [37]
	$Ca_{10}(P_{0.89}As_{0.11}O_4)_6(OH)_2$	24.5_5	535.89		
	$Ca_{10}(P_{0.76}As_{0.24}O_4)_6(OH)_2$	25.3_9	541.59		
	$Ca_{10}(P_{0.57}As_{0.43}O_4)_6(OH)_2$	25.4_7	549.42		
	$Ca_{10}(P_{0.34}As_{0.66}O_4)_6(OH)_2$	25.9_6	558.73		
	$Ca_{10}(P_{0.20}As_{0.80}O_4)_6(OH)_2$	25.5_3	565.37		
	$Ca_{10}(AsO_4)_6(OH)_2$	23.4_6	571.05		
	$Ca_{10}(PO_4)_6F_2$	23.0_6	524.63	The $Ca_{10}(V_{1-x}P_xO_4)_6F_2$ apatites behave in a similar fashion to $Ca_{10}(P_{1-x}As_xO_4)_6(OH)_2$ and again show an increase in φ when the framework is large relative to the tunnel. For many apatites the maximum twist angle that is compatible with $P6_3/m$ symmetry appears to be in the range of $\sim$24–25°. Observations to date suggest that to satisfy bond valence requirements the BO_4 tetrahedron will twist and thereby reduce the symmetry to $P2_1/m$ or $P\bar{1}$. This leads to 3 unique φ for each $A^{I}O_6$ metaprism.	Mercier et al. [16]
	$Ca_{10}(V_{0.10}P_{0.90}O_4)_6F_2$	22.0_9	524.92		
	$Ca_{10}(V_{0.20}P_{0.80}O_4)_6F_2$	23.0_6	533.02		
	$Ca_{10}(V_{0.30}P_{0.70}O_4)_6F_2$	23.1_4	538.04		
	$Ca_{10}(V_{0.40}P_{0.60}O_4)_6F_2$	23.5_4	543.35		
	$Ca_{10}(V_{0.50}P_{0.50}O_4)_6F_2$	23.2_5	550.48		
	$Ca_{10}(V_{0.60}P_{0.40}O_4)_6F_2$	23.6_6	553.65		
	$Ca_{10}(V_{0.70}P_{0.30}O_4)_6F_2$	24.0_8	556.74		
	$Ca_{10}(V_{0.80}P_{0.20}O_4)_6F_2$	24.6_0	562.80		
	$Ca_{10}(V_{0.90}P_{0.10}O_4)_6F_2$	23.9_3	568.36		
	$Pb_{10}(PO_4)_6Cl_2$	18.4_6	634.85	Locating oxygen in apatite structures by X-ray diffraction is challenging. In this series, X-ray scattering is dominated by lead. Therefore the expected trend of an increase in ϕ as larger As^{5+} displaces P^{5+} was not observed. Rather, the twist angles are random. This apatite system may also suffer from oxidation ($2Cl^- \rightarrow O^{2-} + \square$) that would increase metaprism twisting. In addition, the possibility of chemical heterogeneity cannot be ruled out as the materials were treated at low temperatures. Changes in symmetry may also play a role as both hexagonal and monoclinic varieties of natural $Pb_{10}(PO_4)_6Cl_2$ single crystals have been reported [54]. The refinement approach of Mercier et al. [16] to control oxygen trajectories may be useful.	Flis et al. [38]
	$Pb_{10}(As_{0.10}P_{0.90}O_4)_6Cl_2$	19.5_2	638.91		
	$Pb_{10}(As_{0.20}P_{0.80}O_4)_6Cl_2$	17.1_2	643.09		
	$Pb_{10}(As_{0.30}P_{0.70}O_4)_6Cl_2$	18.1_9	647.45		
	$Pb_{10}(As_{0.40}P_{0.60}O_4)_6Cl_2$	17.5_9	652.12		
	$Pb_{10}(As_{0.50}P_{0.50}O_4)_6Cl_2$	17.5_9	656.67		
	$Pb_{10}(As_{0.60}P_{0.40}O_4)_6Cl_2$	18.1_5	661.64		
	$Pb_{10}(As_{0.70}P_{0.30}O_4)_6Cl_2$	19.0_9	665.74		
	$Pb_{10}(As_{0.80}P_{0.20}O_4)_6Cl_2$	19.3_4	670.78		
	$Pb_{10}(As_{0.90}P_{0.10}O_4)_6Cl_2$	20.9_1	674.05		
	$Pb_{10}(AsO_4)_6Cl_2$	19.5_2	677.93		
***X*-type**	$Ca_{10}(PO_4)_6F_2$	23.1_7	523.73	For $Ca_{10}(PO_4)_6(F_{1-x}Cl_x)$ ϕ decreases as larger Cl^- replaces F^-. The doubled unit cell volume arises because there is order correlation of chlorine from tunnel-to-tunnel that is usually modelled as statistically occupancy of an (0 0 z) site in monoclinic $P2_1/b$. The refinement of $Ca_{10}(PO_4)_6Cl_2$ by O'Donnell et al. [39] and Hendricks [9] should be compared.	O'Donnell et al. [39]
	$Ca_{10}(PO_4)_6FCl$	22.2_7	532.42		
	$Ca_{10}(PO_4)_6Cl_2$	18.1_9	1088.05		
	$Ca_{10}(PO_4)_6F_2$	23.2_1	523.08	The data combination of these work showed a linear trend in metaprism twist angle (Fig. 7).	Sudarsanan et al. [53]
	$Ca_{10}(PO_4)_6F_{0.82}Cl_{1.18}$	20.2_1	538.79		Mackie and Young [55]
	$Ca_{10}(PO_4)_6F_{0.34}Cl_{1.66}$	18.6_2	643.13		Mackie and Young [55]
	$Ca_{10}(PO_4)_6Cl_2$	17.8_6	544.50		Sudarsanan and Young [51]

Note: $\square$ = vacancy.

Table 4
Lattice parameters and partitioning coefficient k, for the $[Ba_{10-x}Sr_x][(PO_4)_6][F_2]$ calculated from Aissa et al. [36].

Composition x	0	0.99	3.08	4.95	7.08	8.97	10
a (Å)	10.1611(2)	10.1074(3)	10.0562(5)	9.9288(5)	9.8581(6)	9.7636(3)	9.7211(2)
c (Å)	7.7322(1)	7.6896(2)	7.5939(5)	7.4893(6)	7.3590(4)	7.3258(1)	7.2869(1)
k_{Ba} (A^I/A^{II})[a]	0.67	0.53	0.26	0.18	0.15	0.11	~
R_{wp}	0.069	0.054	0.074	0.047	0.072	0.049	0.084
R_p	0.053	0.039	0.056	0.036	0.065	0.036	0.051

[a] k_{Ba} (A^I/A^{II})=(2*Occ. Fac. Ba(1))/(3*Occ. Fac. Ba(2)); Equal partitioning of Ba over A^I and A^{II} leads to k_{Ba}=0.67.

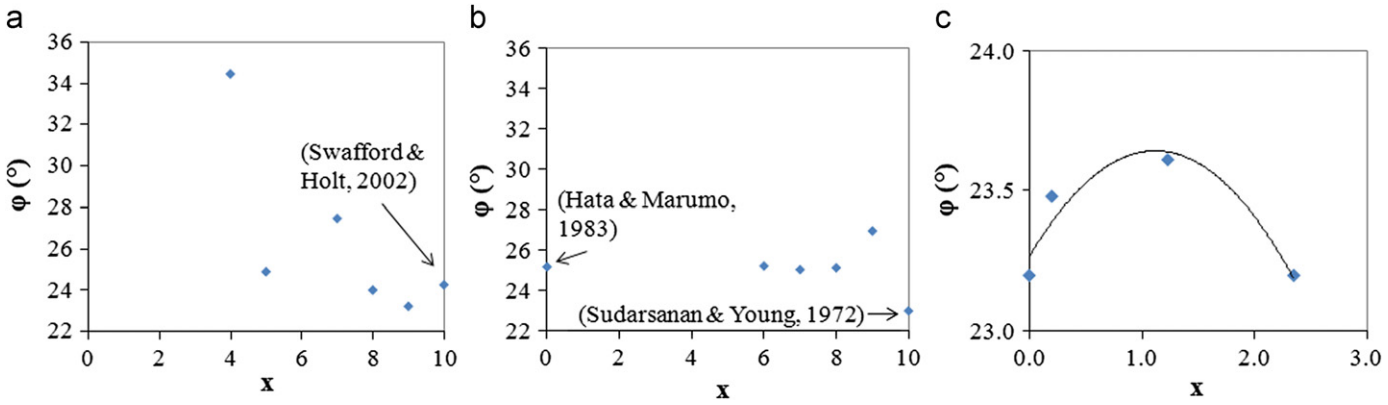

Fig. 5. Metaprism twist angle derived from Badraoui et al. [49] in (a) $[Cd_{10-x}Sr_x][(PO_4)_6][F_2]$, and (b) $[Cd_{10-x}Sr_x][(PO_4)_6][(OH)_2]$. For (c) $[Ca_{10-x}Cd_x][(PO_4)_6][(OH)_2]$ twist angle patterns are collated from Kim et al. [46] and Terra et al. [43].

Table 5
Metaprism twist angle of $[Ca_{10-x}Cd_x][(PO_4)_6][(OH)_2]$.

x Cd	a (Å)	c (Å)	φ (deg.)	Reference
0	9.4322(5)	6.891(2)	23.2_0	Kim et al. [46]
0.2	9.4326	6.8833	23.4_8	Terra et al. [43]
1.23	9.4227	6.9658	23.6_1	Terra et al. [43]
2.349	9.41	6.8448	23.2_0	Terra et al. [43]
10	9.335(2)	6.664(3)	25.8_0	Hata et al. [44]
10	16.1990(3)	6.6485(1)	28.2_1, 21.3_3, 26.4_0 23.2_8, 25.8_8, 26.5_8	Hata and Marumo [45]

of Cd–O bonds results in energetically favoured tenancy of the A^{II} site. The superior crystallographic refinements of Terra et al. [43] support this view via an analysis of twist angle systematics. As Cd^{2+} is smaller than Ca^{2+} the tunnel must contract as cadmium displaces calcium, leading to an increase in φ. In other words, the parabolic trend will be concave up, rather than concave down as in the case of $[Sr_{10-x}Ca_x][(PO_4)_6][F_2]$ (Fig. 5c). Thus for x=0, 0.2, 1.23, 2.349 in $[Ca_{10-x}Cd_x][(PO_4)_6][(OH)_2]$ the twist angle progresses $23.2_0°$, $23.4_8°$, $23.6_0°$ and $23.2_0°$. It is also of note that $P6_3/m$ $[Cd_{10}][(PO_4)_6][(OH)_2]$ [44] yields φ=25.8°. This value appears anomalously high as homoatomic A^I/A^{II} phosphate apatites generally show φ in the range 22–24°. In this regard, it may be significant that in a subsequent paper Hata and Maruro [45] presented a revised supercell for the $Cd_{10}(PO_4)_6(OH)_2$ which was prepared in the presence of minor manganese content that was $P6_3$ (a=16.1990(3) Å, c=6.6485(1) Å) and contains two unique framework A^I sites each with three unique φ (Table 5). An alternate description based on the recent investigation of Baikie et al. [47] may be as a triclinic $P1$ apatite since $Cd_{10}(PO_4)_6(OH)_2$ shows PO_4 tetrahedral tilting reminiscent of $Ca_{10}(PO_4)_6F_2$. While $[Ca_{10-x}Cd_x][(PO_4)_6][(OH)_2]$ solid solutions have been prepared [48] as verified through contraction of the unit cell volume, in the absence of complete structure refinements it is not possible to examine twist angle variations.

Equally, when crystallographic studies yield discontinuities in φ over a solid solution series, or fail to conform to the parabolic trace, changes in composition or symmetry are suspected. For example, using Rietveld analysis Badraoui et al. [49] refined the structures of the fluoro-apatites $[Sr_{10-x}Cd_x][(PO_4)_6][F_2]$, but the metaprism twist angle (Fig. 5a) showed irregularities, especially for $Sr_4Cd_6(PO_4)_6F_2$, where φ=34.4°. This greatly exceeds the maximum twist angle (26.7°) so far observed in any stoichiometric hexagonal apatite for $Pb_{10}(PO_4)_6(OH)_2$ [50]. Similarly, over the limited compositional range reported in the hydroxyl apatite series $[Cd_{10-x}Sr_x][(PO_4)_6][(OH)_2]$ the twist angles reported [49] appear at odds with single crystal determinations of the end members [29,45] (Fig. 5b). As a further example, Bigi et al. [28] reported the twist angles for $Ca_9Sr_1(PO_4)_6(OH)_2$ and $Ca_5Sr_5(PO_4)_6(OH)_2$ grew larger with strontium content, when the opposite behaviour is expected due the favoured introduction of Sr to the tunnel (Table 3). This contrarian observation can be explained if there is oxidation of the X anion ($2OH^- \rightarrow O^{2-} + \square$) that creates tunnel vacancies with a corresponding reduction in diameter and increase in φ.

The twist angles for chlorapatites are less than fluoro- and hydroxyl- analogues as Cl^- is a substantially larger X anion, with the tunnel opening by decreasing φ (Table 3). Sudarsanan and Young [31] examined the $[Ca_{10-x}Sr_x][(PO_4)_6][Cl_2]$ series and determined structures with a parabolic φ trend for differential Ca/Sr site partitioning, but φ=17.8$_6$° for $Ca_{10}(PO_4)_6Cl_2$ is "anomalously" small compared to the $Sr_{10}(PO_4)_6Cl_2$ end member. In this instance, this reflects crystallisation in $P2_1/b$ rather than $P6_3/m$ due to Cl displacements and inter-tunnel correlations. In the original refinement of chlorapatite [9] the symmetry was forced to $P6_3/m$ which led to φ=19.1°, and somewhat closer to $Sr_{10}(PO_4)_6Cl_2$ (21.1°).

Divalent lead (Pb^{2+}) being larger than Ca^{2+} is driven towards tunnel A^{II} positions, and in addition, requires space to accommodate stereochemically active lone pair electrons to produce the expected the parabolic φ trend (Table 3). In lacunar apatites, the tunnels are devoid of X anions (X=□) which must constrict

by increasing φ; consequently, these compounds show the largest φ of all $[A_{10}][(BO_4)_6][X_2]$ apatites (Table 3).

Apatite *A*-site ordering and/or composition can be modified by annealing [35]. For non-equilibrated $Ca_5Pb_5(VO_4)_6F_2$ annealed for 1 day the nominal composition is correct, but the Ca/Pb ions are distributed statistically over the *A* sites. As the average *A* cation size over the framework and tunnel are the same, $\varphi \sim 22^\circ$ and similar to other homoatomic *A*-site apatites e.g. $Sr_{10}(PO_4)_6F_2$. After long annealing (1 week) Ca/Pb order is established, the framework is small relative to the tunnel causing φ to decrease, which is counteracted to a small extent by some loss of fluorine ($2F^- \rightarrow O^{2-} + \square$) which would tend to increase φ.

3.1.2. *B-site correlations*

In $P6_3/m$ apatites the *B*-site is unique. The BO_4 tetrahedron contributes to the framework and for *B*-site substitution φ will vary linearly and become more obtuse as the average ionic size of the *B* ions increases. For example, Lee et al. [37] found the metaprism twist angles in $[Ca_{10}][(P_{1-x}As_xO_4)_6][(OH)_2]$ increased linearly as P^{5+} (0.17 Å) is displaced by As^{5+} (0.335 Å) (Table 3), and the interpretation is straightforward with larger As^{5+} causing the BO_4 tetrahedra to dilate as the *B*–O bond lengths, causing the tunnel to contract and φ to increase [52]. However, for the $Ca_{10}(AsO_4)_6(OH)_2$ end-member φ decreased anomalously, perhaps due to a change of symmetry, although this could not be confirmed in that study. It is noted that the fluoro-analogue $Ca_{10}(AsO_4)_6F_2$ is triclinic [47] and $Ca_{10}(AsO_4)_6(OH)_2$ may be isostructural. In any event, φ systematics suggest the crystal chemistry of the arsenic end member is distinct.

The $Ca_{10}(P_{1-x}V_xO_4)_6F_2$ apatites (Fig. 6) behave in a similar fashion to $Ca_{10}(P_{1-x}As_xO_4)_6(OH)_2$ and again show an increase in φ when the framework is large relative to the tunnel. For many apatites the maximum twist angle that is compatible with $P6_3/m$ symmetry appears to be in the range of $\sim$24–25°. Observations to date suggest that beyond this limit, the BO_4 tetrahedron will twist to satisfy bond valence requirements and thereby reduce the symmetry to $P2_1/m$ or $P\bar{1}$. This leads to 3 unique φ for each A^IO_6 metaprism [47].

The difficulty in locating oxygen accurately in apatites where the metal matrix is a strong X-ray scatterer is illustrated in the $Pb_{10}(P_{1-x}As_xO_4)_6Cl_2$ series [38] (Table 1). Here, the powder X-ray patterns will be dominated by lead resulting in relatively poor sensitivity to oxygen, and possibly errors in occupancy values of the tunnel *X*-site due to the stereographically active Pb^{2+} lone pair electrons directed towards the channel centre. It would be anticipated that as P^{5+} is displaced by larger As^{5+} that φ will increase provided the Pb_6Cl_2 tunnel contents are fixed. The

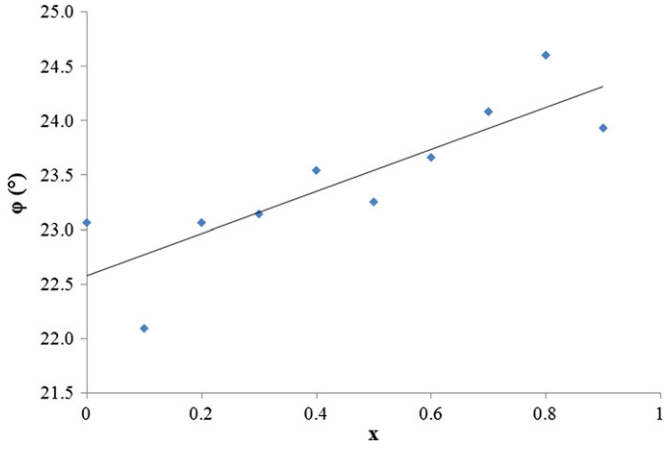

Fig. 6. Metaprism twist angle trend of $[Ca_{10}][(P_{1-x}V_xO_4)_6][(OH)_2]$ by Mercier et al. [16].

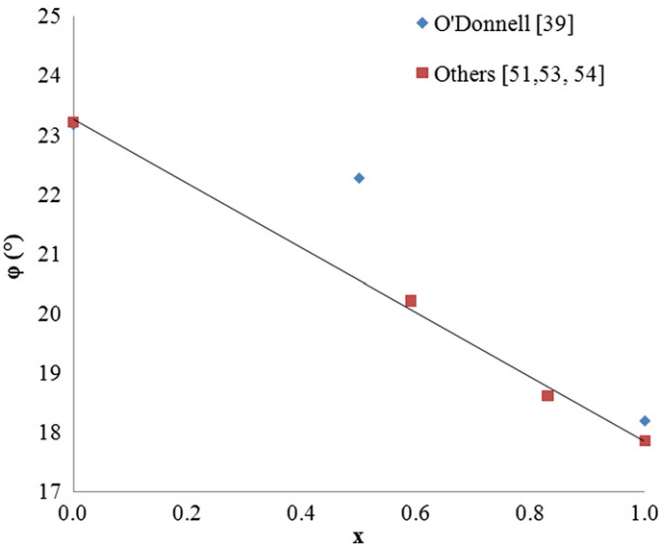

Fig. 7. Metaprism twist angle against atomic percentage of chlorine in $[Ca_{10}][(PO_4)_6][(F_{1-x}Cl_x)_2]$ by O'Donnell et al. [39], Sudarsanan et al. [53], Mackie and Young [55] and Sudarsanan and Young [51].

absence of trend in φ over the series is indicative of poorer refinements, disequilibrium (the materials were produced by a low temperature route), or unexpected compositional variations. For example, where the twist angle appears large relative to single crystal structure determinations of the endmembers it might be suspected that some oxidation has accompanied chlorine volatilization, and in this respect it noted that the oxy analogue $Pb_{10}(PO_4)_6O$ [53] has a relatively larger φ as the tunnel occupancy is half that of the Cl-apatite.

3.2. *X-site correlations*

For $P6_3/m$ apatites there is a single *X* site. Small anions are located at 2*a* (0, 0, 1/4) while larger ions are at 2*b* (0, 0, 0); anions of intermediate size statistically enter 4e (0 0 *z*) positions. For stoichiometric compounds there is linear change in φ. However it is often difficult to prevent halide losses, or the partial inclusion of carbonate or hydroxyls. These changes in chemistry will be reflected in both unit cell parameters and φ. Thus, for $[Sr_{10}][(PO_4)_6][F_{2-x}Cl_x]$, φ decreases as larger Cl^- (1.81 Å) displaces F^- (1.33 Å) causing the tunnel to dilate and the twist angle to reduce, with a linear variation observed in the combined data for metaprism twist angles of Sudarsanan et al. [53], Mackie and Young [55] and Sudarsanan and Young [51] (Fig. 7, Table 3). Similarly, for $[Ca_{10}][(PO_4)_6][(F_{1-x}Cl_x)_2]$ φ decreases as larger Cl^- replaces F^- [39], but the unit cell volume doubles because of order correlation of chlorine from tunnel-to-tunnel that is usually modelled as statistical occupancy of an (0 0 *z*) site in monoclinic $P2_1/b$. More recent work suggests this order is incommensurate [56].

4. Conclusions

Metaprism twist angles can be used as a diagnostic tool to validate apatite structures especially in solid solution series. In this work, the three possible sites for substitutions, namely cationic, metalloid and anionic were considered. The following was demonstrated:

(1) In A^I/A^{II} substitution by divalent ion pairs φ varies in a parabolic fashion due to differences in partitioning co-efficient, with the larger ion entering the 6*h* tunnel position

before occupying the smaller 4*f* framework position. An exception is Cd^{2+} where bonding is more nearly covalent and characteristically enters the A^{II} position.

(2) In *B* substitution the variation in φ is linear, providing there is no change of symmetry. However, for large φ the BO_4 tetrahedra may twist to achieve acceptable bond valence sums and $P2_1/m$ or $P\bar{1}$ polymorphs may result.

(3) In *X* substitution deviations from ideal stoichiometry especially through oxidation and/or volatilization, can be detected, and provide an independent measure of site occupancy.

(4) Where apatites equilibrate slowly during volatilisation or domain formation, φ will continue to be variable until kinetic or thermodynamic equilibrium is reached.

For reliable apatite structures, φ is estimated to have an accuracy better than 0.05°, however a more robust consideration of errors, taking into account not only the precision of the unit cell metric and positional parameters, but also ADP and site occupancy site accuracy would be valuable. This matter is presently under consideration, especially when considering structure–property relationships. Nonetheless, the $A^{I}O_6$ metaprism twist angle provides the means to recognise inferior apatite structure refinements or unanticipated modifications of crystal chemistry. In this paper, the analysis has focused on single site (*A*, *B* or *X*) substitution, but the approach has been extended to multiple *A*/*B*/*X* replacements as found in $[La_{10-x}AE_x][Ge_{6-x}V_x][O_{26+x/2}]$ (AE=Ca, Sr, Ba) solid electrolytes where the ratio of average cation sizes in the tunnel and framework correlate with twist angle and oxygen ion conductivity [57]. This approach has been directly exploited by Kendrick and Slater [58] to design optimised $[La_8Y_2][Ge_{6-x}Ga_x][O_{27-x/2}]$-electrolyte compositions with hexagonal, rather than lower symmetry structures. The location of carbonate in bioapatites controls excipient properties and a recent study of iron-doped hydroxy-carbonate apatite $[Ca_{4-x}Fe_x][Ca_{6-y}(PO_4)_{6-y}(CO_3)_y][(OH_4)_{2-x}(CO_3)_x]$ has demonstrated the value of twist angle systematics for detecting variations in stoichiometry [59]. For $[Sr_2RE_2][RE]_6(SiO_4)_6O_2$ (RE=La, Pr, Tb, Tm, Y) dielectric apatites, being developed for microwave communication devices, modification of φ was associated directly with resonant frequency [60]. Although apatites are under investigation for an increasing range of technologies, the precise control of composition is often challenging, and as demonstrated here, the routine calculation of φ not only provides a rapid method to isolate problematic structural features, but can be used to guide crystallochemical tailoring to enhance physical and chemical properties.

Appendix A. Supplementary materials

Supplementary data associated with this article can be found in the online version at doi:10.1016/j.jssc.2011.08.031.

References

[1] M. Jarcho, J.L. Kay, R.H. Gumaer, H.P. Drobeck, J. Bioeng. 1 (1977) 79–92.
[2] M. Itokazu, W. Yang, T. Aoki, A. Ohara, N. Kato, Biomaterials 19 (1998) 817–819.
[3] S. Nakayama, H. Aono, Y. Sadaoka, Chem. Lett. 24 (1995) 431–432.
[4] A. Smahi, A. Solhy, H.E. Badaoui, A. Amoukal, A. Tikad, M. Maizi, S. Sebti, Appl. Catal. A250 (2003) 151–159.
[5] Y. Xu, F.W. Schwartz, J. Contam. Hydrol. 15 (1994) 187–206.
[6] E.R. Vance, C.J. Ball, B.D. Begg, M.L. Carter, R.A. Day, G.J. Thorogood, J. Am. Ceram. Soc. 7 (2003) 1223–1225.
[7] S.T. Náray-Szabó, Zeits. Kristall. 75 (1930) 387–398.
[8] M. Mehmel, Zeits. Kristall. 75 (1930) 323–331.
[9] S.B. Hendricks, M.E. Jefferson, V. Mosley, Z. Kristallogr. Kristallgeom. Kristallphys. Kristallchem. 81 (1932) 325–369.
[10] T.J. White, C. Ferraris, J. Kim, S. Madhavi, Rev. Mineral. Geochem. 57 (2005) 307–401.
[11] P.H.J. Mercier, Y.L. Page, P.S. Whitfield, L.D. Mitchell, J. Appl. Cryst. 39 (2006) 369–375.
[12] J. Flesche, J. Solid State Chem. 5 (1972) 266–275.
[13] D. McConnell, Springer, Wien, Heidelberg, New York, vol. 111, 1973.
[14] T. Baikie, S.S. Pramana, C. Ferraris, Y.Z. Huang, E. Kendrick, K.S. Knight, Z. Ahmad, T.J. White, Acta Cryst. B66 (2010) 1–16.
[15] P.H.J. Mercier, Y.L. Page, P.S. Whitfield, L.D. Mitchell, I.J. Davidson, T.J. White, Acta Cryst. B61 (2005) 635–655.
[16] P.H.J. Mercier, Z.L. Dong, T. Baikie, Y.L. Page, T.J. White, P.S. Whitfield, L.D. Mitchel, Acta Cryst. B63 (2007) 37–48.
[17] A. Vegas, M. Jansen, Acta Cryst. B58 (2002) 38–51.
[18] T.J. White, Z.L. Dong, Acta Cryst. B59 (2003) 1–16.
[19] R.L. Collin, J. Am. Chem. Soc. 81 (1959) 5275–5278.
[20] R.L. Collin, J. Am. Chem. Soc. 82 (1960) 5067–5069.
[21] Bruker, TOPAS Version 3, Bruker AXS Inc., Madison, WI, USA, 2005.
[22] R.W. Cheary, A. Coelho, J. Appl. Cryst. 25 (1992) 109–121.
[23] R.D. Shannon, Acta Cryst. A32 (1976) 751–767.
[24] S. Hull, R.I. Smith, W.I.F. David, A.C. Hannon, J. Mayers, R. Cywinkski, Physica B 180–181 (1992) 1000–1002.
[25] R.B. Von Dreele, J. Appl. Cryst. 30 (1997) 517–525.
[26] I. Nikčević, V. Jokanović, M. Mitrić, Z. Nedić, D. Makovec, D. Uskoković, J. Solid State Chem. 177 (2004) 2565–2574.
[27] S.H. Swafford, E.M. Holt, Solid State Sci. 4 (2002) 807–812.
[28] A. Bigi, E. Boanini, C. Capuccini, M. Gazzano, Inorg. Chim. Acta 360 (2007) 1009–1016.
[29] K. Sudarsanan, R.A. Young, Acta Cryst. B28 (1972) 3668–3670.
[30] M. Pujari, P.N. Patel, J. Solid State Chem. 83 (1989) 100–104.
[31] K. Sudarsanan, R.A. Young, Acta Cryst. B36 (1980) 1525–1530.
[32] A. Bigi, A. Ripamonti, S. Brückner, M. Gazzano, N. Roveri, S.A. Thomas, Acta Cryst. B45 (1989) 247–251.
[33] M. Azrour., L.E. Ammari, Y.L. Fur, B. Elouadi, J. Solid State Chem. 141 (1998) 373–377.
[34] M.E. Koumiri, S. Oishi, S. Sato, L.E. Ammari, B. Elouadi, Mater. Res. Bull. 35 (2000) 503–513.
[35] Z.L. Dong, T.J. White, K. Sun, L.M. Wangand, R.C. Ewing, J. Am. Ceram. Soc. 88 (2005) 184–190.
[36] A. Aissa, B. Badraoui, R. Thouvenot, M. Debbabi, Eur. J. Inorg. Chem. (2004) 3828–3836.
[37] Y.J. Lee, P.W. Stephens, Y.Z. Tang, W. Li, B.L. Phillips, J.B. Parise, R.J. Reeder, Am. Mineral. 94 (2009) 666–675.
[38] J. Flis, O. Borkiewicz, T. Bajda, M. Manecki, J. Klasa, J. Synch. Rad. 17 (2010) 207–214.
[39] M.D. O'Donnell, R.G. Hill, S.K. Fong, Mater. Lett. 63 (2009) 1347–1349.
[40] E.M. Michie, R.W. Grimes, S.K. Fong, B.L. Metcalfe, J. Solid State Chem. 181 (2008) 3287–3293.
[41] J. Jeanjean, U. Vincennt, M. Fendorf, J. Solid State Chem. 108 (1994) 68–72.
[42] M. Srinivasan, C. Ferraris, T.J. White, Environ. Sci. Technol. 40 (2006) 7054–7059.
[43] J. Terra, G.B. Gonzalez, A.M. Rossi, J.G. Eon, D.E. Ellis, Phys. Chem. Chem. Phys. 12 (2010) 15490–15500.
[44] M. Hata, K. Okada, S. Iwai, Acta Cryst. B34 (1978) 3062–3064.
[45] M. Hata, F. Marumo, Mineral. J. 11 (1983) 317–330.
[46] J.Y. Kim, R.R. Fenton, B.A. Hunter, B.J. Kennedy, Aust. J. Chem. 53 (2000) 679–686.
[47] T. Baikie, P.H.J. Mercier, M.M. Elcombe, J.Y. Kim, Y. Le Page, L.D. Mitchell, T.J. White, P.S. Whitfield, Acta Cryst. B63 (2007) 251–256.
[48] K.J. Zhu, K. Yanagisawa, R. Shimanouchi, A. Onda, K. Kajiyoshi, J. Eur. Ceram. Soc. 26 (2006) 509–513.
[49] B. Badraoui, A. Aissa, A. Bigi, M. Debbabi, M. Gazzano, Mater. Res. Bull. 44 (2009) 522–530.
[50] S. Brueckner, G. Lusvardi, L. Menabue, M. Saladini, Inorg. Chim. Acta 236 (1995) 209–212.
[51] K. Sudarsanan, R.A. Young, Acta Cryst. B34 (1978) 1401–1407.
[52] C.M.B. Henderson, A.M.T. Bell, J.M. Charnock, K.S. Knight, R.F. Wendlandt, D.A. Plant, W.J. Harrison, Mineral. Mag. 73 (2009) 433–455.
[53] K. Sudarsanan, P.E. Mackie, R.A. Young, Mater. Res. Bull. 7 (1972) 1331–1338.
[54] Y.S. Dai, J.M. Hughes, P.B. Moore, Can. Mineral. 29 (1991) 369–376.
[55] P.E. Mackie, R.A. Young, J. Solid State Chem. 11 (1974) 319–329.
[56] F.M. McCubbin, H.E. Mason, H. Park, B.L. Phillips, J.B. Parise, H. Nekvasil, D.H. Lindsley, Am. Mineral. 93 (2008) 210–216.
[57] H. Li, T. Baikie, S.S. Pramana, J.F. Shin, P.R. Slater, F. Brink, J. Hester, K. Wallwork, T.J. White, J. Mater. Chem., under review.
[58] E. Kendrick, P.R. Slater, Mater. Res. Bull. 43 (2008) 3627–3632.
[59] H.R. Low, C. Ritter, T.J. White, Dalton Trans. (2009) 8280–8291.
[60] L.-C. Leu, S. Thomas, M.T. Sebastian, S. Zdzeiszynski, S. Misture, R. Ubic, J. Am. Ceram. Soc. 94 (2011) 2625–2632.